Solar Phys (2017) 292:36
DOI 10.1007/s11207-017-1057-8

Evaluating (and Improving) Estimates of the Solar Radial Magnetic Field Component from Line-of-Sight Magnetograms

K.D. Leka[1] · **G. Barnes**[1] · **E.L. Wagner**[1]

Received: 7 October 2016 / Accepted: 17 January 2017 / Published online: 6 February 2017

Abstract Although for many solar physics problems the desirable or meaningful boundary is the radial component of the magnetic field B_{r}, the most readily available measurement is the component of the magnetic field along the line of sight to the observer, B_{los}. As this component is only equal to the radial component where the viewing angle is exactly zero, some approximation is required to estimate B_{r} at all other observed locations. In this study, a common approximation known as the "μ-correction", which assumes all photospheric field to be radial, is compared to a method that invokes computing a potential field that matches the observed B_{los}, from which the potential field radial component, $B_{\mathrm{r}}^{\mathrm{pot}}$ is recovered. We demonstrate that in regions that are truly dominated by a radially oriented field at the resolution of the data employed, the μ-correction performs acceptably if not better than the potential-field approach. However, it is also shown that for any solar structure that includes horizontal fields, *i.e.* active regions, the potential-field method better recovers both the strength of the radial field and the location of magnetic neutral line.

Keywords Magnetic fields, models · Magnetic fields, photosphere · Active regions, magnetic fields

1. Introduction

Studies of the solar photospheric magnetic field are ideally performed using the full magnetic field vector; for many scientific investigations that may not require the full vector, it is the radial component B_{r} which is often desired, as is derivable from vector observations. Yet observations of the full magnetic vector are significantly more difficult to obtain, from the points of view of both instrumentation and data reduction and analysis, than obtaining maps

---

✉ K.D. Leka
leka@nwra.com

G. Barnes
graham@nwra.com

[1] NWRA, 3380 Mitchell Ln., Boulder, CO 80301, USA

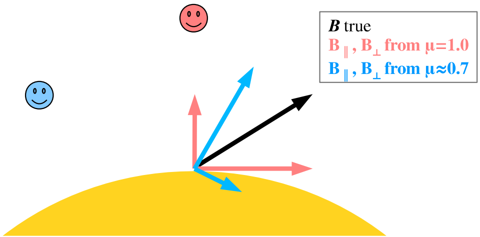

Figure 1 Geometry of projection effects when observing a photospheric magnetic field vector (black) in the image plane, from two different perspectives. Of note regarding the inferred polarity is that the B_{los} component (pointed toward/away from the observer) changes sign between the $\mu = 1.0$ and $\mu = 0.7$ viewing angles.

exclusively of the line-of-sight component of the magnetic field B_{los}. Observations consisting of the line-of-sight component can accurately approximate the radial component only along the Sun–Earth line, that is, where the observing angle $\theta = 0$, or $\mu = \cos(\theta) = 1.0$. Away from that line, *i.e.* at any non-zero observing angle, the line-of-sight component deviates from the radial component. Observing exclusively the line-of-sight component of the solar photospheric magnetic field implies that the observing angle θ imposes an additional difficulty in interpreting the observations – it is not simply that the full strength and direction of the magnetic vector is unknown, but the contribution of these unknown quantities to the B_{los} signal changes with viewing angle. In other words, when $\mu = \cos(\theta) = 1.0$, the line-of-sight component B_{los} is equal to the radial component B_{r}. Nowhere else is this true.

A common approach to alleviate some of this "projection effect" on the inferred total field strength is to assume that the field vector is radial everywhere; then by dividing the observed B_{los} by μ, an approximation to the radial field may be retrieved. This is the "μ-correction". Its earliest uses first supported the hypothesis of the overall radial nature of plage and polar fields, and provided a reasonable estimate of polar fields for heliospheric and coronal magnetic modeling (Svalgaard, Duvall, and Scherrer, 1978; Wang and Sheeley, 1992). However, it was evident from very early studies using longitudinal magnetographs and supporting chromospheric imaging that sunspots were composed of fields that were significantly non-radial, *i.e.* inclined with respect to the local normal. This geometry can lead to the notorious introduction of apparent flux imbalance and "false" magnetic polarity inversion lines (see Figure 1) when the magnetic vector's inclination relative to the line-of-sight surpasses 90° while the inclination to the local vertical remains less than 90°, or *vice versa* (Chapman and Sheeley, 1968; Pope and Mosher, 1975; Giovanelli, 1980; Jones, 1985). Although this artifact can be cleverly used for some investigations (Sainz Dalda and Martínez Pillet, 2005), it generally poses a hindrance to interpreting the inherent solar magnetic structure present.

The inaccuracies that arise from using B_{los} are generally assumed to be negligible when the observing angle θ is smaller than 30°; if the field is actually radial, the correction is only a $\approx 13~\%$ error, and introduced false neutral lines generally appear only in the super-penumbral areas. This is a strong assumption, however, and one known to be inaccurate for many solar magnetic structures. The estimates of polar radial field strength are especially crucial for global coronal field modeling and solar wind estimations (Riley *et al.*, 2006, 2014), but these measurements are exceedingly difficult (Tsuneta *et al.*, 2008; Ito *et al.*, 2010; Petrie, 2015).

The gains afforded by using the full magnetic vector include the ability to better estimate the B_{r} component by way of a coordinate transform of the azimuthally disambiguated inverted Stokes vectors (Gary and Hagyard, 1990). However, although there are instruments now that routinely provide full-disk vector magnetic field data (such as SOLIS, Keller and The Solis Team, 2001; HMI, Hoeksema *et al.*, 2014), the line-of-sight component B_los remains the least noisy, easiest measurement of basic solar magnetic field properties.

We present here a method of retrieving a different, and in the case of sunspots, demonstrably better, estimate of the radial field boundary, $B_\mathrm{r}^\mathrm{pot}$, the radial component of a potential field that is constructed from B_los so as to match to the observed line-of-sight component. This approach was originally described by Sakurai (1982) and Alissandrakis (1981), but is rarely used in the literature. We demonstrate here its implementation, including in spherical geometry for full-disk data. The method is described in Section 2, the data used are described in Section 3, and both the planar and spherical results for $B_\mathrm{r}^\mathrm{pot}$ are evaluated quantitatively for active-region and solar polar areas in Sections 4.1 and 4.2. In Section 4.3 we reflect specifically on the different approximations in the context of "false polarity-inversion line" artifacts, and in Section 4.4 we investigate the reasons behind both regions of success and areas of failure.

2. Method

Approaches to computing the potential field that matches the observed line-of-sight component are outlined here for two geometries, with details given in Appendices A and B. When we focus on a limited part of the Sun such that curvature effects are minimal, a planar approach can be used to approximate the radial field (Section 2.1, Appendix A). The planar approach is fast and reasonably robust for active-region-sized patches (Section 4.1). When the desired radial-field boundary is the full disk or covers an extended area of the disk, such as the polar area, then the spherical extension of the method is the most appropriate (Section 2.2, Appendix B); however, depending on the image size of the input, calculating the radial field in this way can be quite slow.

2.1. Method: Planar Approximation

The line-of-sight component is observed on an image-coordinate planar grid. We avoid having to interpolate to a regular heliographic grid by performing the analysis using a uniform grid in image coordinates, (ξ, η). When we restrict the volume of interest to $0 < \xi < L_x$, $0 < \eta < L_y$ and $z \geq 0$ and neglect curvature across the field of view, the potential field can be written in terms of a scalar potential $\boldsymbol{B}^\mathrm{pot} = \nabla \Phi$, with the scalar potential given by

$$\Phi(\xi, \eta, z) = \sum_{m,n} A_{mn} e^{[2\pi i m\xi/L_x + 2\pi i n\eta/L_y - \kappa_{mn} z]} + A_0 z, \tag{1}$$

where z is the vertical distance above the solar surface. The value of κ_{mn} is determined by $\nabla^2 \Phi = 0$,

$$\kappa_{mn}^2 = (2\pi)^2 \biggl[\bigl(c_{11}^2 + c_{12}^2\bigr) \left(\frac{m}{L_x}\right)^2 + 2(c_{11}c_{21} + c_{12}c_{22}) \left(\frac{m}{L_x}\right)\left(\frac{n}{L_y}\right) + \bigl(c_{21}^2 + c_{22}^2\bigr) \left(\frac{n}{L_y}\right)^2 \biggr], \tag{2}$$

where c_{ij} are the coordinate transformation coefficients given in Gary and Hagyard (1990), and we choose $\kappa_{mn} > 0$ so that the field stays finite at large heights. The values of the coefficients A_{mn} are determined by requiring that the observed line-of-sight component of the field matches the line-of-sight component of the potential field, which results in

$$\begin{aligned}\mathtt{FFT}\big(B^l\big) = L_x L_y A_{jk}\left[\frac{2\pi ij}{L_x}(c_{11}a_{13}+c_{12}a_{23}) + \frac{2\pi ik}{L_y}(c_{21}a_{13}+c_{22}a_{23}) - \kappa_{jk}a_{33}\right] \\ + L_x L_y a_{33} A_0 \delta_{0j}\delta_{0k}, \qquad (3)\end{aligned}$$

where a_{ij} are the elements of the field component transformation matrix given in Gary and Hagyard (1990), and $\mathtt{FFT}(B^l)$ denotes taking the Fourier transform of B^l. The value of A_0 is determined by the net line-of-sight flux through the field of view.

Placing the tangent point at the center of the presented field of view (corresponding to evaluating the coordinate transformation coefficients and the field component transformation matrix at the longitude and latitude of the center of the field of view) is the default, producing a boundary labeled $B_{\mathrm{z}}^{\mathrm{pot,center}}$. The resulting radial component estimation is least accurate near the edges, as expected, and we therefore also present $B_{\mathrm{r}}^{\mathrm{pot,all}}$, for which the tangent point is placed at each pixel presented, the field calculated, and only that pixel's resulting radial field (for which it acted as the tangent point) is included.

2.2. Method: Spherical Case

The potential field in a semi-infinite volume $r \geq R$ can be written in terms of a scalar potential $\boldsymbol{B}^{\mathrm{pot}} = -\nabla\Psi$, given by

$$\Psi = R\sum_{n=1}^{\infty}\sum_{m=0}^{n}\left(\frac{R}{r}\right)^{n+1}\big(g_n^m\cos m\phi + h_n^m\sin m\phi\big)P_n^m(\mu), \qquad (4)$$

where $\mu = \cos\theta$. Defining the coordinate system such that the line-of-sight direction corresponds to the polar axis of the expansion results in particularly simple expressions for the coefficients g_n^m, h_n^m (Rudenko, 2001). However, because observations are only available for the near side of the Sun, it is necessary to make an assumption about the far side of the Sun. The resulting potential field at the surface $r = R$ is not sensitive to this assumption except close to the limb, so for convenience, let $B_l(R, \pi-\theta, \phi) = B_l(R, \theta, \phi)$, where the front side of the Sun is assumed to lie in the range $0 < \theta < \pi/2$.

With these conventions, the coefficients are determined from

$$g_n^m = \begin{cases}\frac{(2n+3)(n-m)!}{2\pi(n+m+1)!}\int_0^{2\pi}d\phi\cos m\phi\int_0^1 d\mu P_{n+1}^m(\mu)B_l(R,\mu,\phi) & n+m \text{ odd}\\ 0 & n+m \text{ even}\end{cases} \qquad (5)$$

and

$$h_n^m = \begin{cases}\frac{(2n+3)(n-m)!}{2\pi(n+m+1)!}\int_0^{2\pi}d\phi\sin m\phi\int_0^1 d\mu P_{n+1}^m(\mu)B_l(R,\mu,\phi) & n+m \text{ odd}\\ 0 & n+m \text{ even}\end{cases} \qquad (6)$$

and the radial component of the field is given by

$$B_r = -\frac{\partial\Psi}{\partial r} = \sum_{n=1}^{\infty}\sum_{m=0}^{n}(n+1)\left(\frac{R}{r}\right)^{n+2}\big(g_n^m\cos m\phi + h_n^m\sin m\phi\big)P_n^m(\mu). \qquad (7)$$

When evaluated at $r = R$, this produces a full-disk radial field boundary designated $B_{\mathrm{r}}^{\mathrm{pot,sph}}$ from which extracted HARPs and polar sub-regions are analyzed below. Our implementation of this approach uses the Fortran 95 SHTOOLS library (Wieczorek *et al.*, 2016) for computing the associated Legendre functions. The routines in this library are considered accurate up to degrees of $n \approx 2800$. For the results presented here, a value of $n = 2048$ was used, corresponding to a spatial resolution of about 2 Mm.

3. Data

For this study we exclusively use the vector magnetic field observations from the *Solar Dynamics Observatory* (Pesnell, 2008) *Helioseismic and Magnetic Imager* (Scherrer *et al.*, 2012; Hoeksema *et al.*, 2014). Two sets of data were constructed: a full-disk test, and a set of HMI Active Region Patches ("HARPs"; Hoeksema *et al.*, 2014, Centeno *et al.*, 2014, Bobra *et al.*, 2014) over five years. To keep comparisons as informative as possible, we construct line-of-sight component data for both from the vector data by transforming the magnetic vector components into a B_{los} map: $B_{\mathrm{los}} = B\cos(\xi)$, where ξ is the inclination of the vector field in the observed plane-of-sky coordinate system, as returned from the inversion.

The full-disk data target is `2011.03.06_15:48:00_TAI`; this date was chosen because of its extreme `B0` angle, which is such that the south pole of the Sun is visible, and also because of the variety of active regions that are visible at low $\mu = \cos(\theta)$ observing angle (away from disk center), and because it has a northern extenion of remnent active-region plage. The `hmi.ME_720s_fd10` full-disk series was used; data are available through the JSOC lookdata tool.[1] Because the weaker fields do not generally have their inherent 180° ambiguity resolved in that series and we evaluate the $B_{\mathrm{r}}^{\mathrm{pot}}$ method in poleward areas of weaker field, two customizing steps were taken. First, a custom noise mask was generated (AMBTHRSH = 0, rather than the default value of 50). Second, a custom disambiguation was performed using the cooling parameters AMBTFCTR = 0.998, AMBNEQ = 200, AMBNGROW = 2, AMBNTX = AMBNTY = 48 (Hoeksema *et al.*, 2014). Compared to the default HMI pipeline implementation, these parameters provide smaller tiles over which the potential field is computed to estimate $d\boldsymbol{B}/dz$, a smaller "buffer" of noisy pixels around well-determined pixels, and slower cooling for the simulated annealing optimization. Disambiguation results were generated for 10 random number seeds. Pixels used for the comparisons shown herein are only those for which both the resulting equivalent of the CONF_DISAMBIG segment is ≥ 60 and for which the results from all 10 random number seeds agreed as well. This requirement translates into 75.3 % of the pixels with CONF_DISAMBIG $\geq$ 60 and 88.8 % of the pixels with CONF_DISAMBIG = 90 being included. There is a 0.2 % chance for our data that the disambiguation solution used results by chance, even in the weak areas (including the poles).

From this full-disk magnetogram the nine identified HARP areas are extracted using the keywords HARPNUM, CRPIX1, CRPIX2, CRSIZE1, and CRSIZE2 from the `hmi.Mharp_720s` series. Two polar regions were also extracted: a "northern plage area", which is an extended remnant field, and a "south pole region" that encompasses the entire visible polar area. A context image is shown in Figure 2, and summary information for each sub-area is given in Table 1, including the WCS coordinates for the two non-HARP regions

---

[1] jsoc.stanford.edu/lookdata.html.

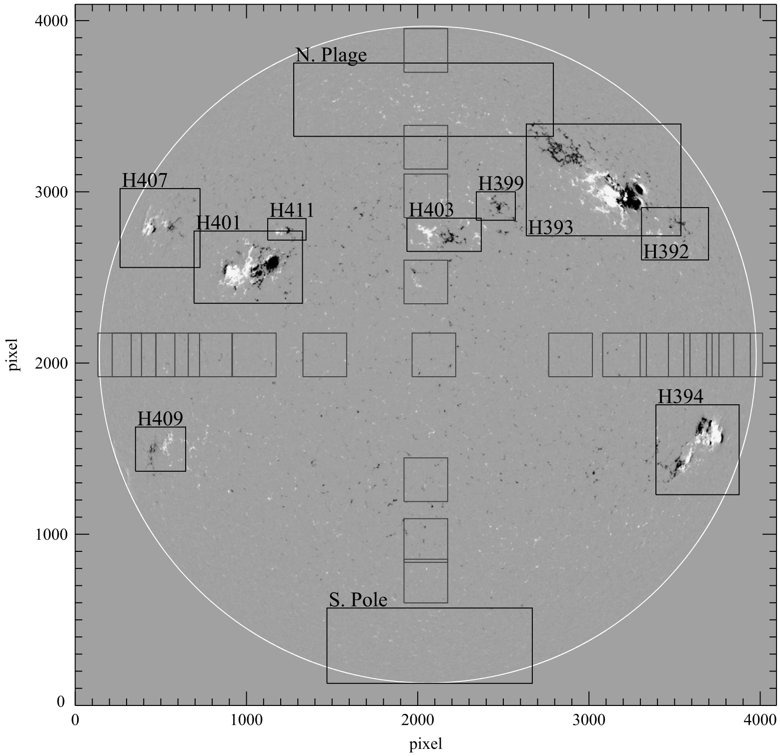

Figure 2 Full-disk image of the line-of-sight component of the solar photospheric magnetic field on 2011 March 6 at 15:48:00_TAI, scaled to ±200 G. The solar limb is indicated, as are the HMI Active Region Patches labeled with their HARP number, and the additional two polar areas used for this analysis. Additional small patches of quiet Sun, distributed in $\mu = \cos\theta$, are indicated as gray boxes that occasionally overlap. Solar north is up, west to the right, and positive or negative directed field is shown as white or black, respectively.

for reproducibility. Table 1 also provides summary data for an additional 22 sub-areas, each 256^2 pixels in size, which are centered along the midpoints in x, y on the image at a variety of $\mu = \cos\theta$ positions.

Throughout this study, we distinguish between invoking planar approximations and accounting for curvature by referring to "B_{z}" and "B_{r}", respectively. The potential-field approximation is performed in three ways, as described in Section 2: using a planar approximation from the center-point coordinates $B_{\mathrm{z}}^{\mathrm{pot,center}}$ of each HARP or extracted sub-region, using a planar approximation with each point of the extracted region used as the center point $B_{\mathrm{r}}^{\mathrm{pot,all}}$, and using the spherical full-disk approach $B_{\mathrm{r}}^{\mathrm{pot,sph}}$. In addition, we calculate two common μ-correction approximations for each sub-region: the center point value of $\mu = \cos(\theta)$ used as a tangent point to obtain $B_{\mathrm{z}}^{\mu} = B_{\mathrm{los}}/\mu$, and second, each pixel's μ value is calculated and applied independently for $B_{\mathrm{r}}^{\mu(s)} = B_{\mathrm{los}}/\mu(s)$, where (s) is the spatial location of the pixel.

The second data set consists of a subset of all HARPs selected over 5.5 years, selected so as to generally not repeat sampling any particular HARP: on days ending with '5' (5th, 15th, and 25th) of all months 2010.05 – 2015.06, the first 'good' (quality flag is 0) HARP set at `:48` past each hour on or after `15:48` was used. HARPs that were defined but for

Table 1 Extracted area descriptions

I.D.	HARP No.	NOAA AR No.	Location	$\mu = \cos(\theta)$	Description
H392	392	11163	N22 W54	0.54	small plage
H393	393	11164	N32 W39	0.65	large complex active region
H394	394	11165	S17 W59	0.49	small active region
H399	399	N/A	N27 W13	0.87	small plage
H401	401	11166	N15 E34	0.79	simple active region
H403	403	11167	N21 W03	0.93	bipolar plage
H407	407	11169	N23 E62	0.43	small active region
H409	409	N/A	S17 E58	0.51	small plage
H411	411	N/A	N22 E27	0.92	small spot
N.Plage	N/A	N/A	N51 E01	0.63	north remnant plage CRPIX1 = 1304 CRPIX2 = 344 CRSIZE1 = 1516 CRSIZE2 = 428
S.Pole	N/A	N/A	S60 E01	0.51	south polar area CRPIX1 = 1199 CRPIX2 = 3527 CRSIZE1 = 1427 CRSIZE2 = 440
QS_E_350	N/A	N/A	N00 E70	0.35	CRPIX1 = 3709 CRPIX2 = 1921
QS_E_450	N/A	N/A	N00 E63	0.45	CRPIX1 = 3625 CRPIX2 = 1921
QS_E_550	N/A	N/A	N00 E57	0.55	CRPIX1 = 3514 CRPIX2 = 1921
QS_E_650	N/A	N/A	N00 E49	0.65	CRPIX1 = 3370 CRPIX2 = 1921
QS_E_750	N/A	N/A	N00 E41	0.35	CRPIX1 = 3181 CRPIX2 = 1921
QS_E_850	N/A	N/A	N00 E32	0.85	CRPIX1 = 2923 CRPIX2 = 1921
QS_E_950	N/A	N/A	N00 E18	0.95	CRPIX1 = 2511 CRPIX2 = 1921
QS_W_1000	N/A	N/A	N00 W01	1.00	CRPIX1 = 1874 CRPIX2 = 1921
QS_W_900	N/A	N/A	N00 W26	0.90	CRPIX1 = 1076 CRPIX2 = 1921
QS_W_800	N/A	N/A	N00 W37	0.80	CRPIX1 = 761 CRPIX2 = 1921
QS_W_700	N/A	N/A	N00 W46	0.70	CRPIX1 = 542 CRPIX2 = 1921
QS_W_600	N/A	N/A	N00 W53	0.60	CRPIX1 = 377 CRPIX2 = 1921
QS_W_500	N/A	N/A	N00 W60	0.50	CRPIX1 = 251 CRPIX2 = 1921
QS_W_400	N/A	N/A	N00 W66	0.40	CRPIX1 = 154 CRPIX2 = 1921
QS_W_300	N/A	N/A	N00 W72	0.30	CRPIX1 = 82 CRPIX2 = 1921
QS_N_375	N/A	N/A	N68 E01	0.375	CRPIX1 = 1921 CRPIX2 = 143
QS_N_775	N/A	N/A	N39 E00	0.775	CRPIX1 = 1921 CRPIX2 = 708
QS_N_875	N/A	N/A	N29 E00	0.875	CRPIX1 = 1921 CRPIX2 = 992
QS_N_975	N/A	N/A	N13 E00	0.975	CRPIX1 = 1921 CRPIX2 = 1495
QS_S_925	N/A	N/A	S22 E00	0.925	CRPIX1 = 1921 CRPIX2 = 2650
QS_S_825	N/A	N/A	S34 E00	0.825	CRPIX1 = 1921 CRPIX2 = 3005
QS_S_725	N/A	N/A	S44 E00	0.725	CRPIX1 = 1921 CRPIX2 = 3242

which there were no active pixels are skipped. The result is 1819 extracted HARPs without regard for size, complexity, or location on the disk. Effectively, the `hmi.Bharp_720s` series was used, including the standard pipeline disambiguation. The NWRA database initially began construction before the pipeline disambiguation was being performed for earlier parts of the mission, thus for some of the data base, the `hmi.ME_720s_fd10` data were used, the HARP regions extracted, and the disambiguation performed in-house, matching the implementation performed in the HMI pipeline. All analysis is performed up to 80° from disk center, and only points with significant signal-to-noise ratio (S/N) in the relevant components ($\mathrm{S/N} > 3$ relative to the returned uncertainties from the inversion, and propagated accordingly) are included in the analyses. For this larger data set, all calculations are performed with a planar approximation. The "answer" is B_z, and the boundary estimates calculated are $B_\mathrm{z}^{\mu} = B_\mathrm{los}/\mu$, $B_\mathrm{r}^{\mu(s)} = B_\mathrm{los}/\mu(s)$ (which imparts a spherical accounting as a result of the variation of μ over the field of view), and $B_\mathrm{z}^\mathrm{pot,center}$. $B_\mathrm{r}^\mathrm{pot,all}$ and $B_\mathrm{r}^\mathrm{pot,sph}$ are computationally possible but extremely slow, and are not employed for this second data set.

4. Results

For the results presented here, the "gold standard" is taken to be the radial or normal field as computed from the vector data, and to this quantity we compare results of different approximations of the boundary. We do caution that B_r data include the observed B_trans component, which is inherently noisier than the B_los component. Additionally, we stress that the comparisons are performed against a particular instrument's retrieval of the photospheric magnetic field vector, which may not reflect the true Sun due to influences in polarimetric sensitivity, spectral finesse, spatial resolution, *etc.*

4.1. Field Strength Comparisons

To demonstrate the general resulting trends for each of the radial field approximations, we first present density histograms of the inferred radial field strengths for two representative sub-regions, NOAA AR 11164 (HARP #393, Figure 3) and the south pole region (Figure 4). Throughout, we do not indicate the errors for clarity; a 10 % uncertainty in field strength is a fair approximation overall, and a detailed analysis beyond that level is not informative here.

For both HARP `H393` (NOAA AR 11164) and the south pole area, the initial comparison of B_los to B_r (panel (a) in Figures 3 and 4) shows the expected signature of underestimated field strengths overall. Note that for both regions, but especially for the south pole, there is a strong underestimation of the radial field strength across magnitudes.

The $B_\mathrm{r}^{\mu(s)}$ correction (panel (b) in Figures 3 and 4; the B_z^{μ} plot is almost identical and not shown here) shows improvement by eye for both regions, with distributions systematically deviating less from the $x = y$ line. However, in the case of the `H393` corrections, the stronger-field strengths are often over-corrected, and the opposite-polarity erroneous pixels are exacerbated in their error. This trend is also true for the south pole area: there is both an improvement (especially for stronger-field points) and the appearance of a distinct erroneous opposite-polarity spur in the $B_\mathrm{r}^{\mu(s)}$ results.

In the next panel (panel (c) in Figures 3 and 4), a representative potential-field option, $B_\mathrm{z}^\mathrm{pot,center}$, is shown with regard to B_r (again, the $B_\mathrm{r}^\mathrm{pot,sph}$ and $B_\mathrm{r}^\mathrm{pot,all}$ plots look essentially identical); the weaker-field strengths appear to be less well corrected than the $B_\mathrm{r}^{\mu(s)}$ approximation, although the strong-field approximations for the sunspots in `H393` are significantly better than the $B_\mathrm{r}^{\mu(s)}$ correction. There appears to be a small number of points for which the opposite polarity is retained, but the stronger-field points (generally ≥ 1000 G) lie overall close to the $x = y$ line. There are still significant deviations from the B_r field; this is expected

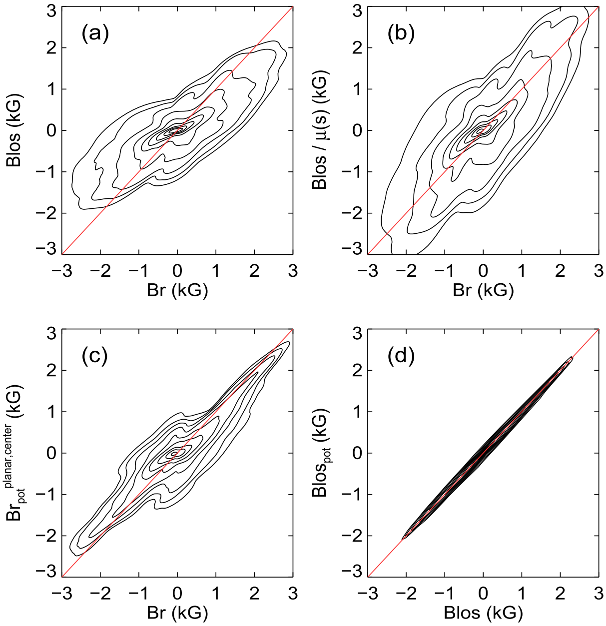

Figure 3 (a) – (c) Non-parametric density estimates comparing the distribution of the radial field from the vector field data B_r (x-axis) to the inferred radial field strength estimates using representatives of the different models discussed in the text (y-axis). Shown here are distributions from NOAA AR 11164 (`H393`). Contour levels are equal in log (probability) ranging from $[10^{-3}–10^{2}]$, with $x = y$ line included for reference. The comparisons are for B_r against (a) B_los, (b) $B_\mathrm{los}/\mu(s)$, (c) B_z potential, planar, center-point pivot. Panel (d) shows, in summary, that the μ-corrected estimates generally show less bias than the B_los fields, but still have a large random error. The potential-field-corrected fields show larger differences for weak-field strengths, but less random error. In (d) the scatter plot is between the B_los calculated from the inversion, and the recovered B_los calculated from the spherical potential vector (Sect. B). While the boundary is thus fairly well recovered, the disagreement beyond machine-precision differences arises because the spherical calculation is not performed to a high enough degree to remove all small-scale "ringing".

at some level since a potential-field model is being imposed, and it cannot be expected that the solar magnetic fields are in fact potential. Additionally, while a nonlinear force-free field model may better represent the true field (Livshits *et al.*, 2015), there is insufficient information in the B_los boundary with which to construct such a model. For the south pole region, the strong-field areas are less well corrected than was seen in the $B_\mathrm{r}^{\mu(s)}$ plot (Figure 4, panels (c) and (b)), but the distinct incorrect-polarity spur visible for $B_\mathrm{r}^{\mu(s)}$ is less pronounced in the potential-field-based estimate.

For completeness and as a check of the algorithm, the B_los directly attained from the inversion as $B_\mathrm{los} = |\boldsymbol{B}| \cos(\xi)$, where ξ is the inclination of the field vector to the line of sight (and which constitutes the input to the potential-field calculation), is compared with the $B_\mathrm{los}^\mathrm{pot}$ derived from the vector field components from the derived potential field (panel (d) in Figures 3 and 4). These B_los boundaries match well, indicating that there is little if any systematic bias presented by the potential-field calculation when recovering the input boundary. The recovery is not, however, within machine precision because of the lower-than-optimal degree to which the spherical potential field is computed; reproducing the boundary to machine precision is computationally untenable with this algorithm.

Figure 4 Same as Figure 3, but for the south pole area shown in Figure 2. These panels show in summary, that the μ-corrected estimates for the south polar area show distinct spurs with incorrect polarity, while the potential-field estimates have large biases.

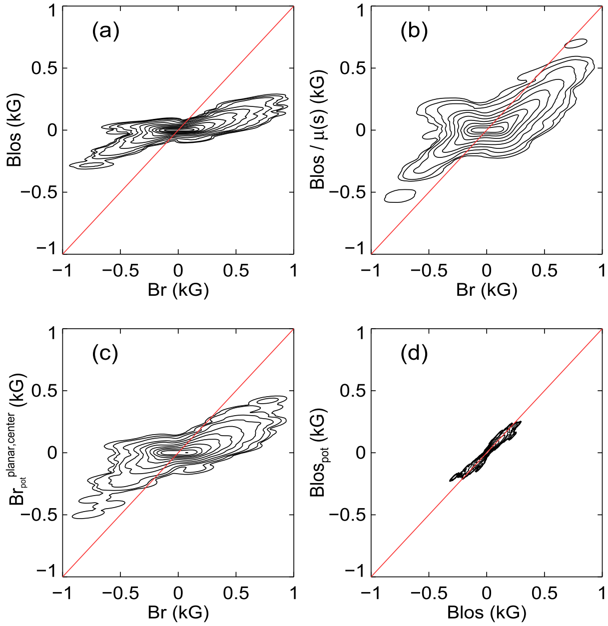

The two examples shown in Figures 3 and 4 represent the two extremes of solar magnetic features to which these approximations would be applied: the south polar region (expected to sample small, primarily radially-directed concentrations of field) and a large active region with both plage and sunspots. The distributions of the other sub-regions appear as hybrids when examined in the same manner, having sometimes stronger fields for which the μ-correction approach performs the best (*e.g.*, the northern plage area), or having sunspot areas for which there is an incorrect-polarity spur present in the distributions that is exacerbated by some amount in the μ-corrections and mitigated by some amount with the potential-field calculations.

To summarize, the performance of these approaches, quantitative metrics of the comparisons between B_r and the different estimations for the sub-regions on 2011 March 6 are graphically presented in Figures 5, 6, and 7 for all HARP-based sub-regions plus the north and south targets considered, and in Figure 8 for the small quiet-Sun extractions. The metrics considered are the linear correlation coefficient, the fitted linear regression slope and constant, a mean signed error, a root-mean-square error, and the percentage of pixels that show the incorrect sign relative to B_r. All well-measured points within each sub-region are considered in Figure 5 (see Section 3), and in Figures 6 and 7 the results are separated between strong- and weaker-field areas as well.

It is clear is that there is not a single best approach. In some cases, *e.g.* for `H394` and `H407`, by almost all measures the $B_\mathrm{r}^\mathrm{pot,sph}$ and $B_\mathrm{z}^\mathrm{pot,center}$ approaches improve upon B_los and the μ-correction methods. The latter generally show less bias than the uncorrected B_los field, but still have a large random error. The potential-field-based estimates show larger differences for weak-field strengths, but less random error. Comparing the weak- and strong-field results, it is clear that the small correlations and regression slopes in the former are due to the abundance of weak-field points and their low response to the corrections (see Figure 3 *vs.* 4). However, there is a general trend that plage- or weaker-field dominated areas, including the two polar areas, are better served (under this analysis) by the μ-correction methods, notwith-

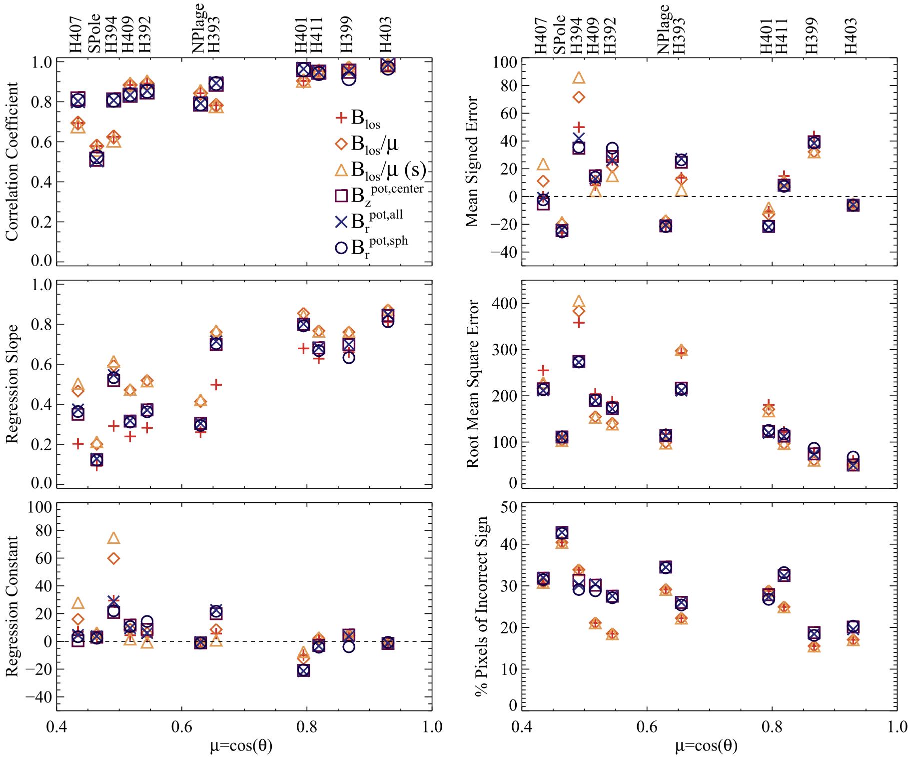

Figure 5 Metrics used to evaluate the performance of radial-field approximations when compared to B_{r}, for the cut-out areas highlighted in Figure 2. Top to bottom, left: the linear correlation coefficient, the slope of the linear regression line, the constant (offset) for that fit, and right: the mean error, the root-mean-square error, the percent of pixels that are of the incorrect sign. In shades of orange, +: B_{los}, ◇: B_{z}^{μ}, △: $B_{\mathrm{r}}^{\mu(s)}$; in shades of purple, □: $B_{\mathrm{z}}^{\mathrm{pot,center}}$, ×: $B_{\mathrm{r}}^{\mathrm{pot,all}}$, ○: $B_{\mathrm{r}}^{\mathrm{pot,sph}}$. These metrics demonstrate some trends (less spread between methods with increasing μ), but also a mix of results between regions, μ, and methods, indicating no single best approach.

standing the polarity-sign errors. This is confirmed as a general trend by the quiet-Sun areas (Figure 8) whose underlying structures – like the polar area and plage areas – are likely predominantly radial in HMI data. In contrast, when the sub-areas include or are dominated by sunspots, (*e.g.*, `H393, H394, H401, H407`), the $B_{\mathrm{r}}^{\mathrm{pot,sph}}$ and $B_{\mathrm{z}}^{\mathrm{pot,center}}$ perform best by these metrics. The reasons behind this mixed message of success is explored further below.

The quiet-Sun patches are sampled in order to exclusively test the dependence of the approximations to μ, without the complications of different underlying structure: we assume these comprise similar samples of small primarily radial magnetic structures. Indeed, Figure 8 shows clear trends with μ. All models improve with increasing μ by these metrics, and there is no obvious difference in trends between quadrants (east, north, *etc.*). There are outliers that are most likely due to inherent underlying structure. The μ-correction methods generally better serve these areas, by a small degree in some measures, than the potential-field methods. However, all regions except those with $\mu \approx 1.0$ have a higher percentage of points with the incorrect sign than all of the HARP regions, except for the south polar area.

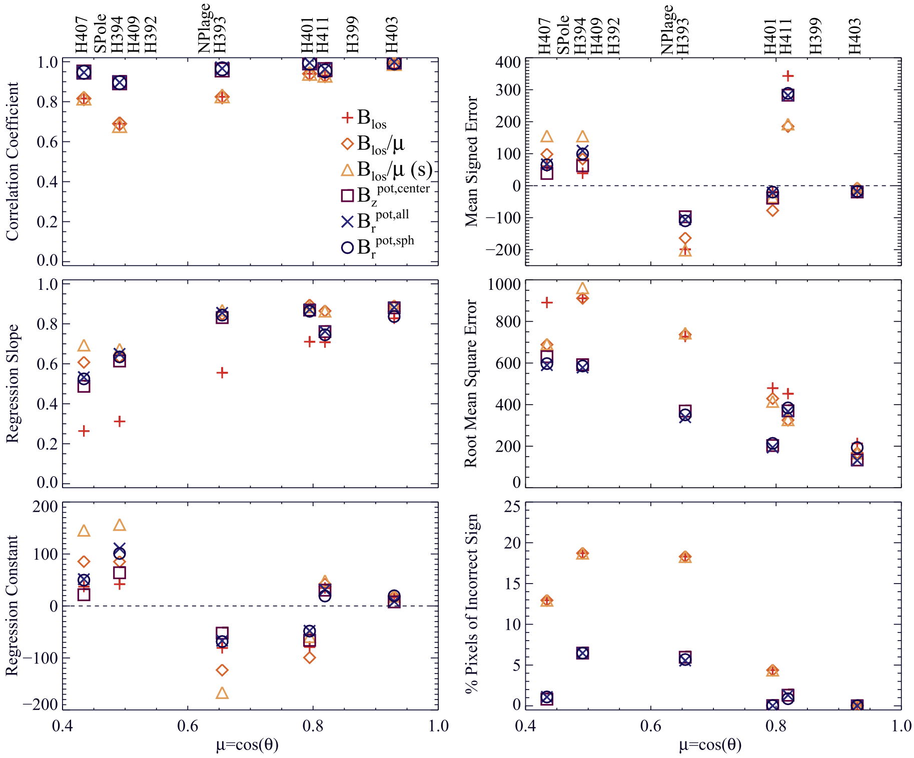

Figure 6 Same as Figure 5, but only for points with total field strengths $|\boldsymbol{B}| > 1000$ G (note the different scales from previous figures for some metrics). As some of the sub-regions do not meet the additional restriction of having a minimum of 100 such points, they are not included in this plot. Note that compared with Figure 5, there are in some cases stronger distinctions between the method categories, and much weaker relationships with $\mu = \cos(\theta)$ for some metrics.

4.2. Total Flux Comparisons

The second test is the total magnetic flux of the sub-regions, where the estimates of the magnetic flux are computed as $\sum |\mathrm{B}_{\mathrm{bndry}}| d\mathrm{A}$ over the acceptable pixels, dA is the area in Mm^2 of each pixel (thus imparting some spherical accounting for the flux, which otherwise uses a planar approximation), and $\mathrm{B}_{\mathrm{bndry}} = B_{\mathrm{los}},\ B_{\mathrm{z}}^{\mu},\ B_{\mathrm{z}}^{\mathrm{pot,center}}$ or similar, as indicated. The results are summarized in Figure 9, both for all well-measured pixels and then for strong-field (sunspot) pixels alone. The results for the regions extracted from the full-disk data are considered first.

Overall, the total flux estimate using $\Phi(B_{\mathrm{r}})$ is always the largest, the estimate using $\Phi(B_{\mathrm{los}})$ is always the smallest, with other approximations in varying order between. As demonstrated in Section 4.1, the behaviors can be quite mixed between strong-field sunspot areas, and plage areas, making the summations over the entire sub-regions (for the total flux) difficult to interpret. It is also clear that the degree of underestimation of the B_{los}-based flux $\Phi(B_{\mathrm{los}})$ is a function of μ, and the flux from the B_{z}^{μ} boundaries recover the $\Phi(B_{\mathrm{r}})$ for the same data well overall. The fluxes based on potential-field-based boundaries do not completely recover $\Phi(B_{\mathrm{r}})$ either, even when the area under consideration is restricted to the

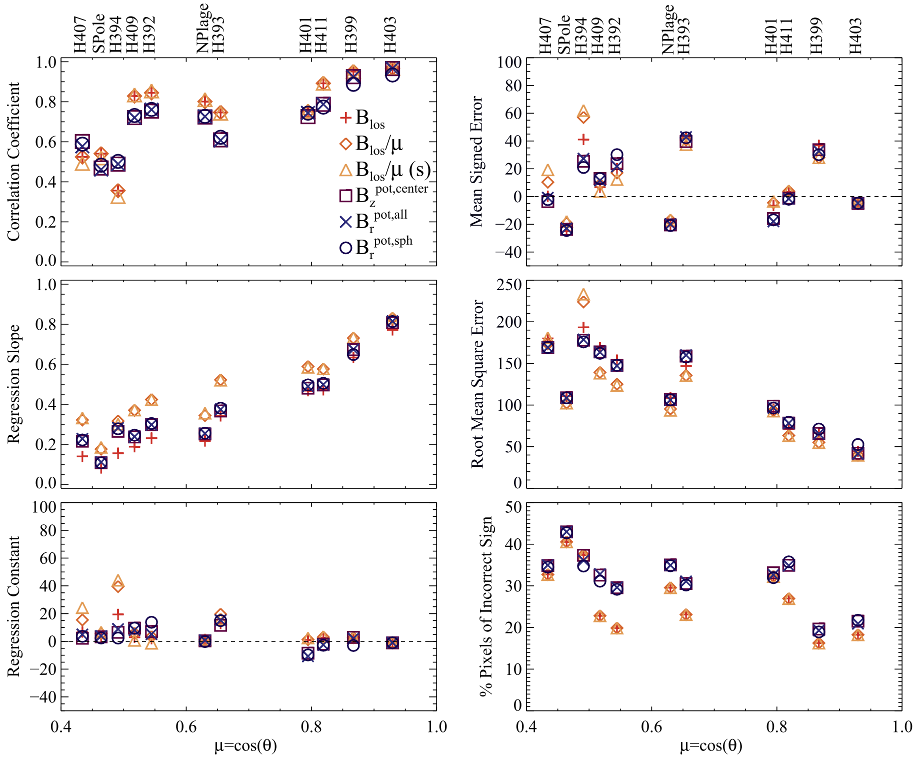

Figure 7 Same as Figure 5, but only for points with $B_h < 500$ G and $|B_r| < 500$ G (note the different scales for some metrics). Some metrics once again show a strong relationship with μ, and again there is a weaker trend between the method categories.

sunspots. The different implementations of each method do not vary significantly between each other.

Furthermore, a close examination of Figure 9 as compared to Figure 3 shows something that is slightly confusing: while Figure 3 shows regions of the distribution where $|B_{los}| > |B_r|$ and certainly $|B_{los}|/\mu > |B_{los}|$, in Figure 9 $\Phi(B_r) > \Phi(B_{los})$ and indeed $\Phi(B_r) > \Phi(B_r^{\mu(s)})$ always. The differences decrease with increasing μ, as noted above. With a non-trivial number of points having $|B_{los}| > |B_r|$, however, the question is why the total flux would be consistently higher when computed using B_r? The answer is that B_r includes the higher-noise component B_{trans}, whereas any estimation using B_{los} does not include that higher-noise component. The impact is much greater in weak-signal areas that dominate the summation for the total flux when all points are used (Figure 9, left) and the impact is less when only strong-field points are included (Figure 9, right). This impact of photon noise on B_{trans} and its particular influence on the calculation of $\Phi(B_r)$ *vs.* $\Phi(B_{los})$ is confirmed using model data with varying amount of photon noise (Leka *et al.*, 2009). While in this context we consider B_r the “answer”, it is therefore clear that it instead exclusively represents an observed estimate against which we compare other estimates, and is likely to be an overestimate of the true flux.

The larger HARP database is used next to examine the $\Phi(\mathrm{B_{bndry}})$ differences for a large number of extracted regions (Figure 10). In this plot, the general underestimation of $\Phi(B_r)$ by $\Phi(B_{los})$ is present as expected, and varies with $\mu = \cos(\theta)$; $\Phi(B_z^{\text{pot,center}})$ also underesti-

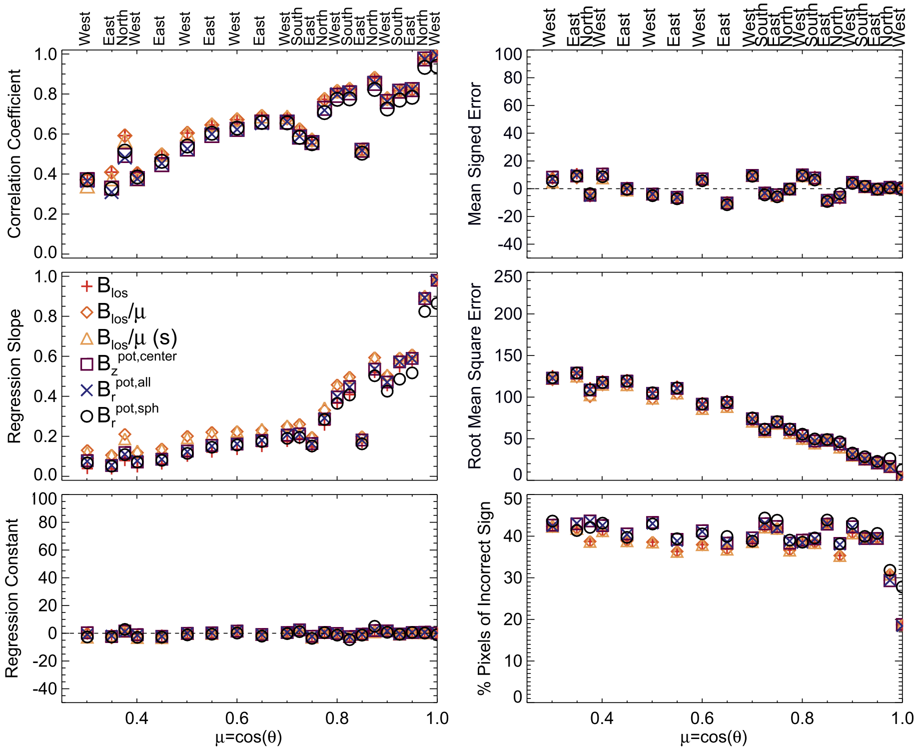

Figure 8 Same as Figure 5, but for the small quiet-Sun extractions at a thorough sampling of μ. The top label indicates the quadrant from which the extraction originated.

mates the flux relative to $\Phi(B_{\mathrm{r}})$ although not as severely, and the consistently larger $\Phi(B_{\mathrm{r}})$ is now understood, from the comments above regarding the inherent influence of noise. $\Phi(B_{\mathrm{r}}^{\mu(s)})$ is closer to $\Phi(B_{\mathrm{r}})$ for much of the range in observing angle, but it is also capable of overestimating the total flux, from relatively modest through large observing angles; this is a property not generally seen when using the $B_{\mathrm{z}}^{\mathrm{pot,center}}$ boundary. Using $\Phi(B_{\mathrm{los}})$ therefore results in the largest systematic error, while $\Phi(B_{\mathrm{r}}^{\mu(s)})$ results in the smallest systematic error, with $\Phi(B_{\mathrm{z}}^{\mathrm{pot,center}})$ showing an intermediate systematic error relative to $\Phi(B_{\mathrm{r}})$. For the random error, the converse order holds, with $\Phi(B_{\mathrm{r}}^{\mu(s)})$ resulting in the largest random error, $\Phi(B_{\mathrm{los}})$ the smallest, with the $\Phi(B_{\mathrm{z}}^{\mathrm{pot,center}})$ random error comparable to $\Phi(B_{\mathrm{los}})$.

4.3. Magnetic Polarity Inversion Lines

The introduced apparent magnetic polarity changes at the edges of sunspots were very early signatures that inclined structures are prevalent in active regions. For many solar physics investigations, however, the location of and character of the magnetic field nearby the magnetic polarity inversion line (PIL) is central to the analysis. In particular, magnetic PILs with locally strong gradients in the spatial distribution of the normal field are often of interest as an indication of localized very strong electric currents that are associated with subsequent solar flare productivity (Schrijver, 2007). Incorrect neutral lines introduced by projection may misidentify limb-ward penumbral areas as being strong-gradient regions of interest.

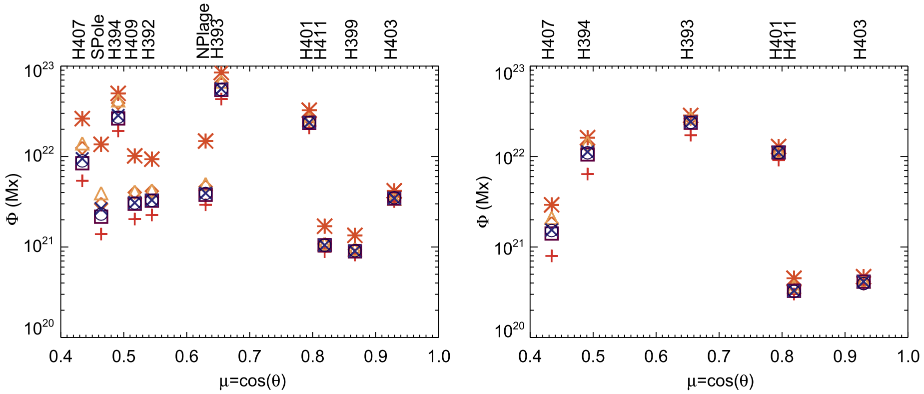

Figure 9 A comparison of inferred total magnetic flux $\Phi = \sum |B_{bndry}| dA$ for each sub-region as a function of the observing angle, using different radial-field approximations for the B_r boundary; for all, dA is the area in Mm^2 of each pixel (thus imparting some spherical accounting for calculations that might otherwise use a planar approximation). Left: all points in each sub-region, right: only points with total field strengths over 1000 G (which removes some sub-regions from consideration). For both, the symbols and colors follow Figure 5 with the addition of $*$: B_r (red).

Figure 10 Scatterplot of the differences in total flux when computed using B_{los}, $B_r^{\mu(s)}$, and $B_z^{pot,center}$ as indicated, as a percentage difference from the total flux computed using B_r (capped at 100 % difference), as a function of observing angle $\mu = \cos(\theta)$ (limited to $\theta \leq 80°$ from disk center).

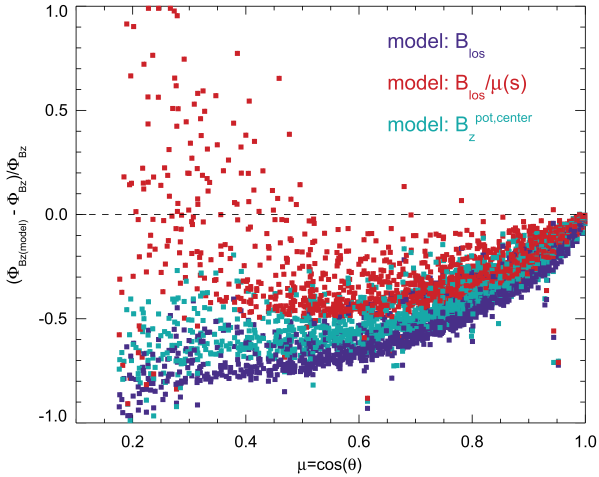

Figure 11 shows images of the observed B_r field, then the analogous estimates from B_{los}, B_z^{μ}, and $B_z^{pot,center}$ for `H393` in detail; this sunspot group is fairly large, complex, and quite close to the limb. In particular, areas of strong-gradient neutral lines are highlighted. The location of the implied magnetic neutral line clearly does not change at all when the B_z^{μ} correction is applied to the B_{los} boundary, as expected from a simple scaling factor, but the highlighted areas do change because the magnitude of the gradient increases. The $B_z^{pot,center}$ boundary better replicates the B_r boundary, almost completely removing the introduced polarity lines on the limb-ward sides of the sunspots. However, it is not perfect: there is a slight decrease in the magnitude of the field in the negative-polarity plage area that extends toward north/east of the active region. This is in part due to a planar approximation being invoked, but also due to the introduction of inclined fields by the potential-field model where the underlying field inferred by HMI is predominantly vertical (see Section 4.4).

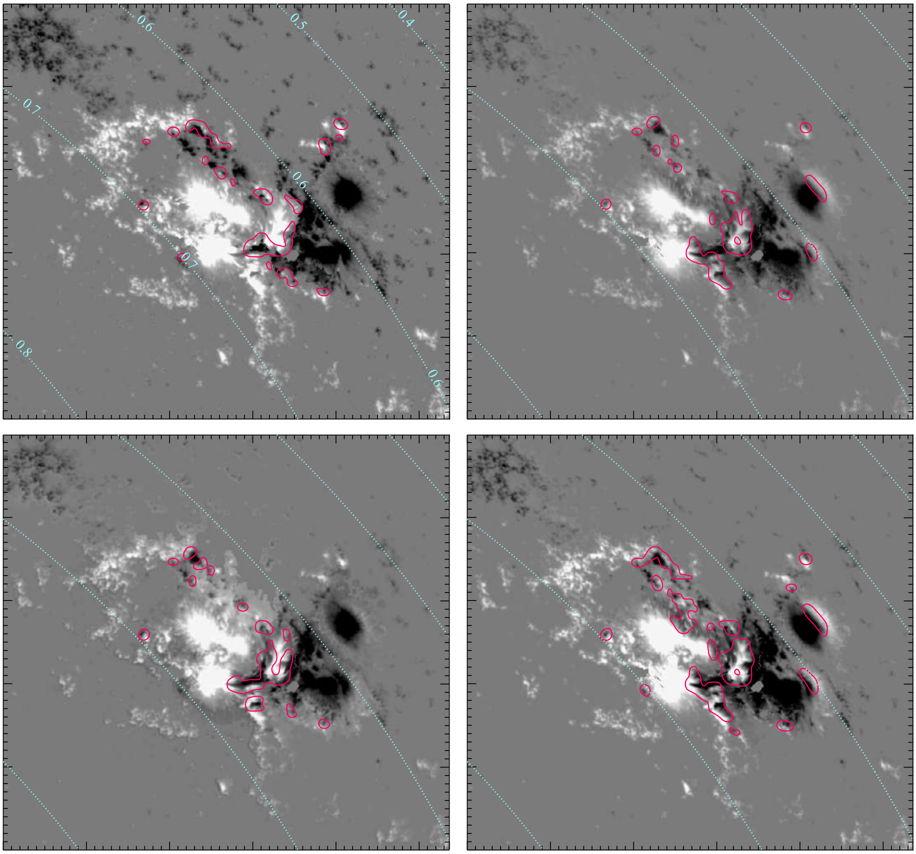

Figure 11 Images of the boundary magnetic field for NOAA AR 11164 (a sub-area of HARP 393; *cf.* Figure 2), scaled to ±1 kG, positive or negative (white or black). The inferred strong-gradient PILs are shown (red contours); also indicated are $\mu = \cos(\theta)$ at 0.1-spaced intervals (teal). Top, left and right: The radial field B_{r} (with μ contours labeled) and the line-of-sight field B_{los}. Bottom, left and right: The radial component of the potential field that matches B_{los} on the boundary, using a planar approximation $B_{\mathrm{z}}^{\mathrm{pot,center}}$, and the line-of-sight field with the μ-correction B_{z}^{μ}.

The recovery of a more appropriate PIL in or near sunspots with polarity errors in weaker fields was seen earlier in the analysis of the points of incorrect sign in Figures 5 – 7. The strong-field regions showed a significant decrease in incorrect-polarity fields when a potential-field-based boundary was used relative to the μ correction boundaries, but in the weak-field areas the results were mixed, leading to a similarly mixed result when all pixels were included.

4.4. Analysis of Success and Failure

While it is clear that the location of the magnetic neutral line is better recovered for sunspot areas away from disk center using a potential-field model than is possible using the B_{los} boundary and a multiplicative factor, it is also clear that there are indeed some solar structures for which the potential-field model does not perform well.

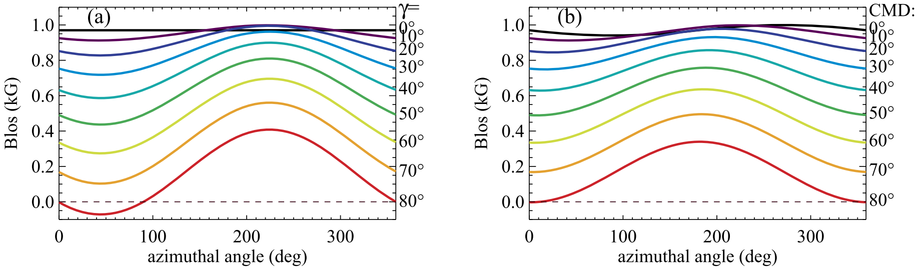

Figure 12 Variations in expected B_{los} signal from a magnetic vector with $|\boldsymbol{B}| = 1000$ G, located at N10, as a function of inherent azimuthal angle ϕ, while varying (a) the inclination angle γ (keeping the heliographic longitude at W10), and (b) varying the heliographic longitude and thus the observing angle (keeping the inherent inclination angle at 10°).

We investigate where the different approximations work well and where they do not, based on the hypothesis that the μ-correction approach should be exactly correct (by construction) for truly radial fields as inferred within the limitations of the instrument in question.

First, it behooves us to recall that the B_{los} component of a magnetic field vector itself can vary widely for a given magnitude $|\boldsymbol{B}|$ as a function of the observing angle θ, the *local* inclination angle γ (relative to the *local* normal), and the local azimuthal angle ϕ. Conventional practices of assuming that errors are within acceptable limits when a target B_{los} is within, say, 30° of disk center, may be surprisingly misleading when the expected B_{los} magnitude is so significantly different from the input vector magnitude, as demonstrated in Figure 12. The impact of the azimuthal angle as well as the inclination angle on the observed B_{los} explains some of why the μ-correction based estimates of the radial field may impart greater errors than might be expected. In other words, one should expect (for example) a 20 % introduced uncertainty in the B_{los} component relative to the inherent field strengths even at $\theta = 30°$ simply because of the unknown azimuthal directions of the underlying horizontal component of the field – as contrasted to an estimated 13 % error from simply geometric considerations at this observing angle.

To explore more where the different approaches fail, and how, an analysis of the difference between the B_{r} approximations and the B_{z} component from the vector field observations is performed in detail for one HMI Active Region Patch. HARP 3848, observed by HMI on 2014 March 15 at 15:48:00 TAI includes NOAA AR 12005 and AR 12007 (Figure 13), and was centered northeast of disk center; it is one of the regions and days included in the larger HARP data set, and was chosen because of its location, its relatively simple main sunspot plus a second sunspot at a different μ value, and because it includes a spread of plage over a fair range of μ as well. The differences between the observed radial component (in this case all using planar approximations) B_{z} and two different B_{r} approximations, from $B_{\mathrm{r}}^{\mu(s)}$ and $B_{\mathrm{z}}^{\mathrm{pot,center}}$ are examined for points in very restrictive local inclination ranges as a function of structure and observing angle. Two representations are shown: the absolute magnitude (Figure 14), and the fractional difference (Figure 15); the points that resulted in an erroneous sign change (relative to the B_{z} boundary) are also indicated. Only points that have a good disambiguation and have $\mathrm{S/N} > 5$ are included.

Summarizing both plots, for $\gamma < 10°$, the $B_{\mathrm{r}}^{\mu(s)}$ approximation is systematically closer to B_{z} than the $B_{\mathrm{z}}^{\mathrm{pot,center}}$ results; this is especially true in plages for the $B_{\mathrm{r}}^{\mu(s)}$ model, which also shows no sign-error points, whereas there are a few sign-error points in the $B_{\mathrm{z}}^{\mathrm{pot,center}}$ model. For $20° < \gamma < 30°$, slightly inclined fields, the bulk of the points are less different

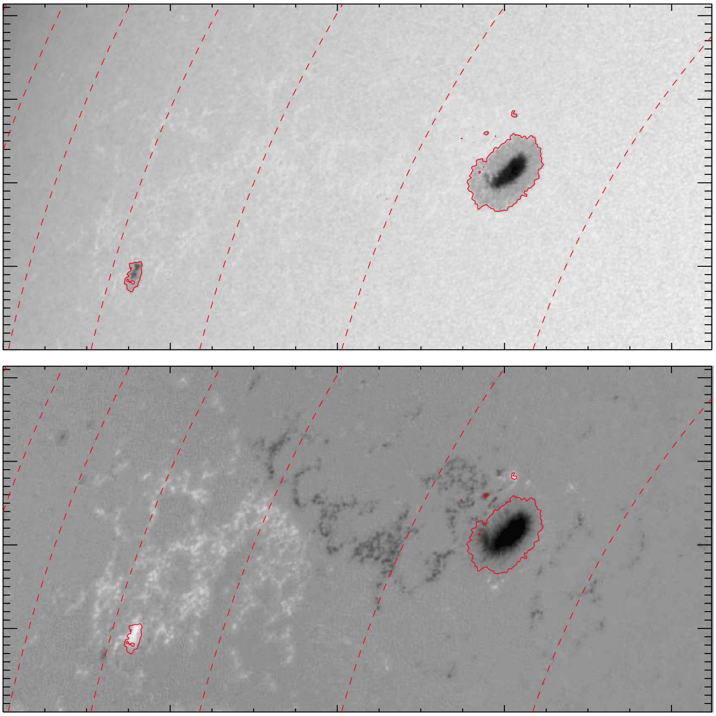

Figure 13 HARP 3848 (NOAA AR 12005, 12007), obtained at 2014 March 15 at 15:48:00 TAI. Top: continuum intensity, bottom: radial field B_{z}, positive and negative polarity as white and black and scaled to ±2 kG; red contours indicate 0.9 times the median of the continuum intensity and indicate the sunspots, red dashed contours delineate $\mu = [0.3, 0.4, 0.5, 0.6, 0.7, 0.8]$; for reference to Figure 14.

between the two boundaries, but it is most striking that the $B_{\mathrm{r}}^{\mu(s)}$ approximation is beginning to show significant differences in the sunspots, whereas the $B_{\mathrm{z}}^{\mathrm{pot,center}}$ sunspot areas continue to display fairly small errors. The latter do, however, show a greater number of plage points that have introduced an erroneous polarity difference, whereas $B_{\mathrm{r}}^{\mu(s)}$ only shows these errors at the more extreme μ values. When we examine only points within $40^\circ < \gamma < 50^\circ$ range – significantly inclined, but not horizontal – the errors in the spot become very large in $B_{\mathrm{r}}^{\mu(s)}$, but stay consistent and small in the $B_{\mathrm{z}}^{\mathrm{pot,center}}$ boundary. More points in the former are also of the incorrect sign, including many with quite large field-strength differences. The $B_{\mathrm{z}}^{\mathrm{pot,center}}$ boundary in fact performs better for both plage and spots at these larger inclination angles than $B_{\mathrm{r}}^{\mu(s)}$.

The appropriateness of a μ-correction in the context of vertical fields is shown thus to be true, but surprisingly limited to a very small degree of deviation *away* from truly vertical. By 20° from vertical, the results are mixed. For more inclined fields, the $B_{\mathrm{r}}^{\mu(s)}$ is clearly problematic, particularly in sunspots (in part due to the (unknown) inherent azimuthal angle), but also in inclined weak-field areas. One must note, however, that what are inferred to be weak-field inclined points may be predominantly a product of noise in the vector field data at these larger observing angles. The $B_{\mathrm{z}}^{\mathrm{pot,center}}$ boundary is demonstrably better for all inclinations within sunspots, and is susceptible to polarity errors in weak-field areas at all inclinations but at a somewhat more consistent, lower level. In this particular case, the percentage of plage-area pixels with incorrect sign (over all inherent inclination angles) is lower for the

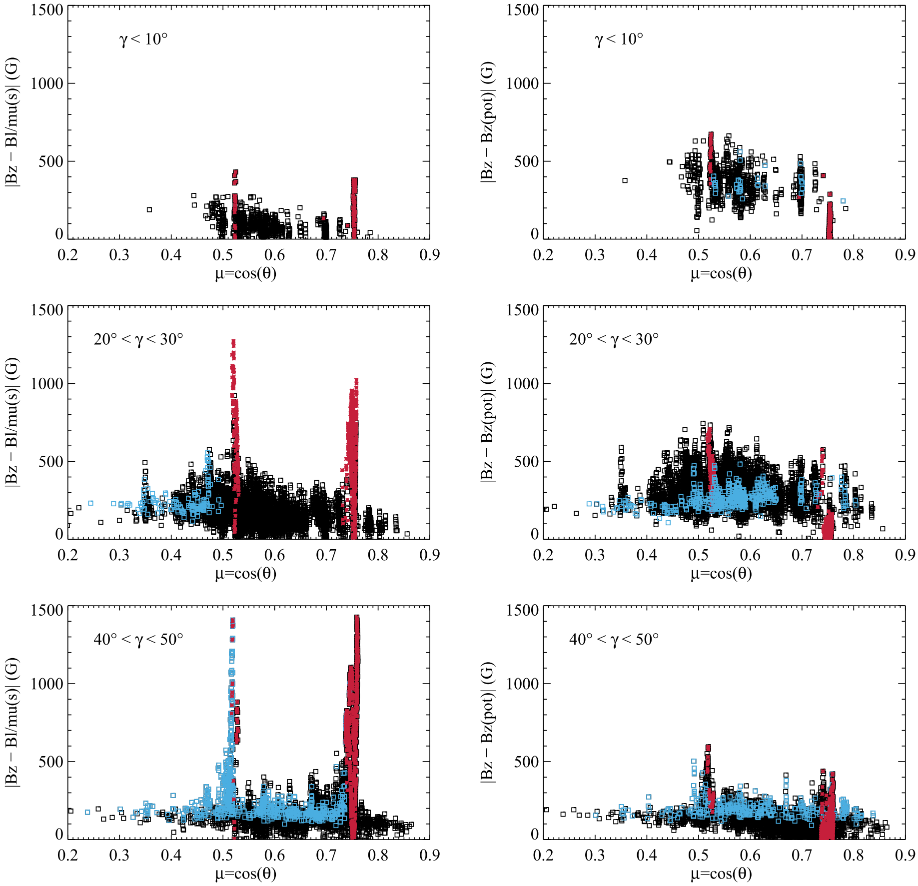

Figure 14 Top: absolute difference between B_{z} and $B_{\mathrm{r}}^{\mu(s)}$ (left), and $B_{\mathrm{z}}^{\mathrm{pot,center}}$ (right), as a function of $\mu = \cos(\theta)$, only for points with a local inclination angle γ smaller than 10° from radial. Points that lie within the spots are indicated by an asterisk (red). Pixels for which the model resulted in a different sign of the field are further highlighted by overplotting the squares in blue. Middle: the same, but for points $20° < \gamma < 30°$; bottom: the same, but for points with $40° < \gamma < 50°$.

$B_{\mathrm{z}}^{\mathrm{pot,center}}$ boundary than the $B_{\mathrm{r}}^{\mu(s)}$ (6.1 % *vs.* 11 %, respectively), and the former appears to perform quantitatively better for both plage and spot areas in this example.

5. Conclusions

A method was developed, based on earlier publications (Sakurai, 1982; Alissandrakis, 1981), and was tested here for its ability to produce an estimate of the radial field distribution from line-of-sight magnetic field observations of the solar photosphere. Comparisons were made between the line-of-sight component calculated from the vector-field observations, the inferred radial-directed component from same, and different implementations of two approaches for estimating the radial component from line-of-sight observations: one approach based on the common μ-correction, and one based on using the radial field component from

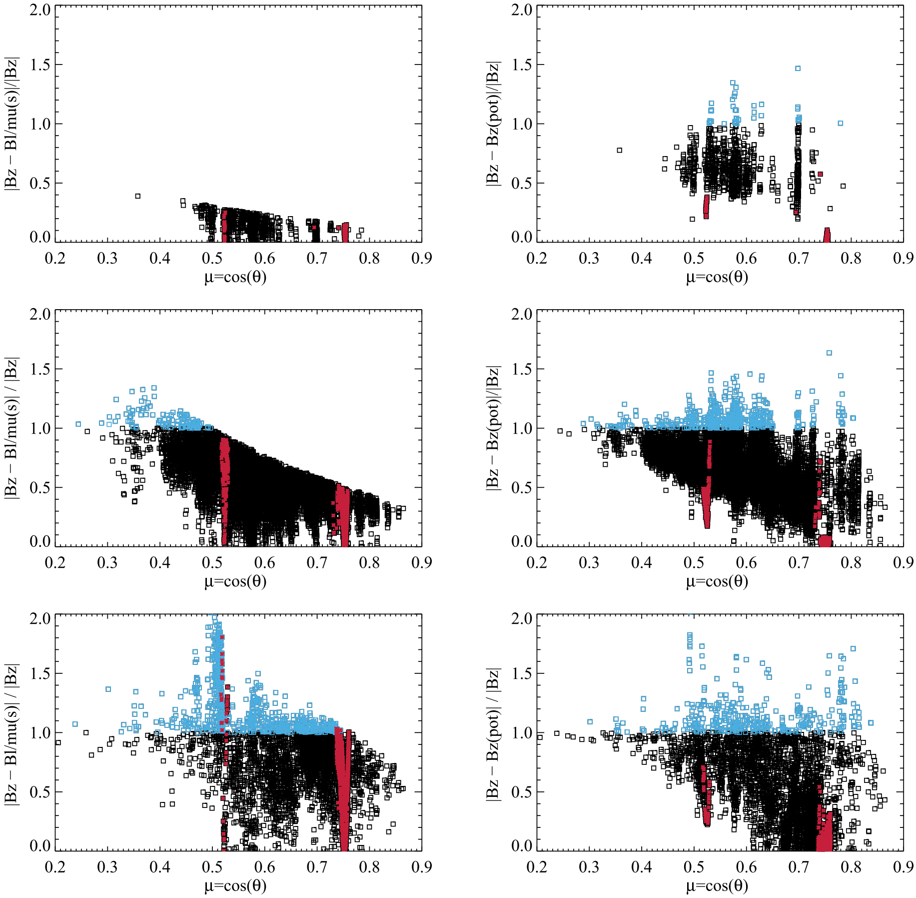

Figure 15 Same as Figure 15, but each difference is normalized by $|B_Z|$ to show the fractional change. Points with a sign error (blue square overplot) therefore all show a change of at least 100 %.

a potential field constructed so as to match the line-of-sight input. The potential-field constructs impose, of course, significant assumptions regarding the underlying structure. The μ-correction approach imposes a single much stronger assumption: that the underlying field is always directed normal to the local surface.

We find that answering the question of which approach better recovers a target quantity differs according to said target's underlying magnetic field structure, as would be inferred by the instrument at hand. Structures that abide by the radial-field assumption are well recovered by μ-correction approaches. This may, with caution, be extended to structures whose inherent inclination is up to a few tens of degrees, but with an uncertain worsening error as a function of increasing observing angle. Magnetic structures that would be observed to be inherently more inclined by that instrument are generally poorly served by μ-correction approaches.

Most active regions comprise a mix of structures, and making general performance statements is therefore dangerous. While sunspot field strengths are far better recovered using the potential-field constructs, tests on polar or high-latitude areas that should be primarily plage tell a mixed story: higher field strengths are recovered more reliably using some form of μ-correction, but the results also indicate that a significant subset of the measurements are returned with the incorrect magnetic polarity. That being said, the total magnetic flux, an extensive quantity that often encompasses all structures within an active region, can be better recovered by μ-correction approaches *if* the target is dominated by a field that would be expected to be inferred as radial by the instrument involved.

B_los images of sunspots often have pronounced "false" magnetic polarity inversion lines; because the μ-correction approaches involve multiplying by a simple scaling factor, they cannot relocate incorrect PILs and instead enhance incorrect-polarity field strengths. This is a particular problem when strong-gradient PILs need to be identified. The potential-field approaches can mitigate the false-PIL problem; the impact was demonstrated on a near-limb active region, but PIL displacement can occur at any location where $\mu \neq 1.0$.

Of course it can be argued that the potential field is not appropriate for magnetically complex active regions, and that linear or nonlinear extrapolations would perform even better. Unfortunately, without crucial additional constraints, there is no unique linear or nonlinear force-free field solution to the B_los boundary, whereas the potential field provides a unique solution.

The most general conclusions are that first, any correction improves upon the naive $B_\mathrm{los} = B_\mathrm{r}$ approach. Second, the μ-corrections recover field strengths in areas inherently comprised of vertical structures (as would be inferred by the instrument), but introduce random errors whose magnitude can be surprisingly large given a sunspot's proximity to disk center, and these corrections exacerbate the influence of projection-induced sign errors. Last, while the potential-field reconstructions will introduce systematic errors, generally underestimating field strengths and introducing new polarity-sign errors in weaker and more radially directed fields, it recovers well both the radial-component field strengths in sunspots and the locations of the magnetic polarity inversion lines.

Acknowledgements The authors would like to acknowledge the helpful comments by the referee for this manuscript. The development of the potential-field reconstruction codes and the preparation of this manuscript was supported by NASA through contracts NNH12CH10C, NNH12CC03C, and grant NNX14AD45G. This material is based upon work supported by the National Science Foundation under Grant No. 0454610. Any opinions, findings, and conclusions or recommendations expressed in this material are those of the author(s) and do not necessarily reflect the views of the National Science Foundation.

Disclosure of Potential Conflicts of Interest The authors declare that they have no conflicts of interest.

Appendix A: Method: Planar Approximation

The line-of-sight component is observed on an image-coordinate planar grid. To avoid having to interpolate to a regular heliographic grid, consider a hybrid (non-orthogonal) coordinate system, (ξ, η, z^h), consisting of the transverse image components, (ξ, η) and the heliographic normal component, z^h.

Following the convention of Gary and Hagyard (1990), the coordinates ξ, η are defined in the $z^h = 0$ plane in terms of heliographic coordinates by

$$\begin{pmatrix} \xi \\ \eta \end{pmatrix} = \begin{pmatrix} c_{11} & c_{12} \\ c_{21} & c_{22} \end{pmatrix} \begin{pmatrix} x^h \\ y^h \end{pmatrix}, \tag{8}$$

thus the new coordinate system is related to helioplanar coordinates by

$$\begin{pmatrix} \xi \\ \eta \\ z^h \end{pmatrix} = \begin{pmatrix} c_{11} & c_{12} & 0 \\ c_{21} & c_{22} & 0 \\ 0 & 0 & 1 \end{pmatrix} \begin{pmatrix} x^h \\ y^h \\ z^h \end{pmatrix}. \tag{9}$$

Hence, the calculations are performed in the coordinate system (ξ, η, z), which is *not* the same as the image coordinates, except at $z = 0$. As such, there will be three coordinate systems under consideration, related as follows. The heliographic and image coordinates are related by the standard transform given in Gary and Hagyard (1990):

$$\begin{pmatrix} x^h \\ y^h \\ z^h \end{pmatrix} = \begin{pmatrix} a_{11} & a_{12} & a_{13} \\ a_{21} & a_{22} & a_{23} \\ a_{31} & a_{32} & a_{33} \end{pmatrix} \begin{pmatrix} x^i \\ y^i \\ z^i \end{pmatrix}, \tag{10}$$

while the new coordinate system is related to the originals by

$$\begin{aligned} \begin{pmatrix} \xi \\ \eta \\ z \end{pmatrix} &= \begin{pmatrix} c_{11} & c_{12} & 0 \\ c_{21} & c_{22} & 0 \\ 0 & 0 & 1 \end{pmatrix} \begin{pmatrix} x^h \\ y^h \\ z^h \end{pmatrix}, \\ &= \begin{pmatrix} c_{11}a_{11} + c_{12}a_{21} & c_{11}a_{12} + c_{12}a_{22} & c_{11}a_{13} + c_{12}a_{23} \\ c_{21}a_{11} + c_{22}a_{21} & c_{21}a_{12} + c_{22}a_{22} & c_{21}a_{13} + c_{22}a_{23} \\ a_{31} & a_{32} & a_{33} \end{pmatrix} \begin{pmatrix} x^i \\ y^i \\ z^i \end{pmatrix}. \end{aligned} \tag{11}$$

Henceforth, the superscript on the heliographic components is dropped, but retained on the image components.

The volume of interest is restricted to $0 < \xi < L_x$, $0 < \eta < L_y$ and $z \geq 0$. Assuming that c_{ij} is constant (that is, neglecting curvature across the field of view), this transformation is linear and the solution to Laplace's equation should still be of the form

$$\Phi(\xi, \eta, z) = \sum_{m,n} A_{mn} e^{[2\pi i m\xi/L_x + 2\pi i n\eta/L_y - \kappa_{mn} z]} + A_\xi \xi + A_\eta \eta + A_0 z, \tag{12}$$

with the value of κ_{mn} determined by $\nabla^2 \Phi = 0$, namely

$$\begin{aligned} \nabla^2 \Phi(\xi, \eta, z) &= \frac{\partial^2 \Phi}{\partial \xi^2}\left[\left(\frac{d\xi}{dx}\right)^2 + \left(\frac{d\xi}{dy}\right)^2\right] + 2\frac{\partial^2 \Phi}{\partial \xi \partial \eta}\left[\frac{d\xi}{dx}\frac{d\eta}{dx} + \frac{d\xi}{dy}\frac{d\eta}{dy}\right] \\ &\quad + \frac{\partial^2 \Phi}{\partial \eta^2}\left[\left(\frac{d\eta}{dx}\right)^2 + \left(\frac{d\eta}{dy}\right)^2\right] + \frac{\partial^2 \Phi}{\partial z^2} \\ &= \sum_{m,n} A_{mn} e^{[2\pi i m\xi/L_x + 2\pi i n\eta/L_y - \kappa_{mn} z]} \left\{ \left(c_{11}^2 + c_{12}^2\right)\left(\frac{2\pi i m}{L_x}\right)^2 \right. \\ &\quad + 2(c_{11}c_{21} + c_{12}c_{22})\left(\frac{2\pi i m}{L_x}\right)\left(\frac{2\pi i n}{L_y}\right) \\ &\quad \left. + \left(c_{21}^2 + c_{22}^2\right)\left(\frac{2\pi i n}{L_y}\right)^2 + \kappa_{mn}^2 \right\} \\ \Longrightarrow \quad \kappa_{mn}^2 &= (2\pi)^2 \left[\left(c_{11}^2 + c_{12}^2\right)\left(\frac{m}{L_x}\right)^2 + 2(c_{11}c_{21} + c_{12}c_{22})\left(\frac{m}{L_x}\right)\left(\frac{n}{L_y}\right) \right. \\ &\quad \left. + \left(c_{21}^2 + c_{22}^2\right)\left(\frac{n}{L_y}\right)^2 \right], \end{aligned} \tag{13}$$

and we choose $\kappa_{mn} > 0$ so that the field decreases with height. We also choose $A_\xi = A_\eta = 0$ so that the constant field is purely vertical. This is equivalent to specifying the boundary condition at large heights.

The line-of-sight component of the field is thus given by

$$\begin{aligned} B_l &= \frac{\partial}{\partial x_l}\left\{\sum_{m,n} A_{mn} e^{2\pi i m\xi/L_x + 2\pi i n\eta/L_y - \kappa_{mn} z} + A_0 z\right\} \\ &= a_{33} A_0 + \sum_{m,n} A_{mn} e^{2\pi i m\xi/L_x + 2\pi i n\eta/L_y - \kappa_{mn} z} \\ &\quad \times \left[\frac{2\pi i m}{L_x}(c_{11}a_{13} + c_{12}a_{23}) + \frac{2\pi i n}{L_y}(c_{21}a_{13} + c_{22}a_{23}) - \kappa_{mn} a_{33}\right]. \end{aligned} \tag{14}$$

We solve for the coefficients A_{mn} by taking the Fourier transform of the line-of-sight component of the field at the surface

$$\begin{aligned} \mathtt{FFT}\big(B^l\big) &= \int_0^{L_x} d\xi \int_0^{L_y} d\eta\, B_l(\xi, \eta, 0) e^{-2\pi i j\xi/L_x - 2\pi i k\eta/L_y} \\ &= \sum_{m,n} A_{mn}\left[\frac{2\pi i m}{L_x}(c_{11}a_{13} + c_{12}a_{23}) + \frac{2\pi i n}{L_y}(c_{21}a_{13} + c_{22}a_{23}) - \kappa_{mn} a_{33}\right] \\ &\quad \times \int_0^{L_x} d\xi \int_0^{L_y} d\eta e^{2\pi i(m-j)\xi/L_x + 2\pi i(n-k)\eta/L_y} \\ &\quad + A_0 \frac{\partial z}{\partial x_l}\int_0^{L_x} d\xi \int_0^{L_y} d\eta\, e^{-2\pi i j\xi/L_x - 2\pi i k\eta/L_y} \\ &= L_x L_y A_{jk}\left[\frac{2\pi i j}{L_x}(c_{11}a_{13} + c_{12}a_{23}) + \frac{2\pi i k}{L_y}(c_{21}a_{13} + c_{22}a_{23}) - \kappa_{jk} a_{33}\right] \\ &\quad + L_x L_y a_{33} A_0 \delta_{0j}\delta_{0k}. \end{aligned} \tag{15}$$

When the coefficients are known, the vertical component of the field is then given by

$$\begin{aligned} B_z(\xi, \eta, 0) &= \frac{\partial}{\partial z}\left\{\sum_{m,n} A_{mn} e^{2\pi i m\xi/L_x + 2\pi i n\eta/L_y - \kappa_{mn} z} + A_0 z\right\}\Bigg|_{z=0} \\ &= A_0 - \sum_{m,n} \kappa_{mn} A_{mn} e^{2\pi i m\xi/L_x + 2\pi i n\eta/L_y}. \end{aligned} \tag{16}$$

Appendix B: Method: Spherical Case

Following the derivation given in Altschuler and Newkirk (1969), but also see Bogdan (1986), the potential field in a semi-infinite volume $r \geq R$ can be written in terms of a scalar potential given by

$$\Psi = R \sum_{n=1}^{\infty}\sum_{m=0}^{n}\left(\frac{R}{r}\right)^{n+1}\big(g_n^m \cos m\phi + h_n^m \sin m\phi\big) P_n^m(\mu), \tag{17}$$

where $\mu = \cos\theta$, in terms of which the heliographic components of the field are given by

$$\begin{aligned} B_r &= -\frac{\partial\Psi}{\partial r} \\ &= \sum_{n=1}^{\infty}\sum_{m=0}^{n}(n+1)\left(\frac{R}{r}\right)^{n+2}\big(g_n^m \cos m\phi + h_n^m \sin m\phi\big)P_n^m(\mu), \end{aligned} \tag{18}$$

$$\begin{aligned} B_\theta &= -\frac{1}{r}\frac{\partial\Psi}{\partial\theta} \\ &= \frac{1}{\sin\theta}\sum_{n=1}^{\infty}\sum_{m=0}^{n}\left(\frac{R}{r}\right)^{n+2}\big(g_n^m \cos m\phi + h_n^m \sin m\phi\big) \\ &\quad \times \big[(n+1)\mu P_n^m(\mu) - (n-m+1)P_{n+1}^m(\mu)\big] \end{aligned} \tag{19}$$

$$\begin{aligned} B_\phi &= -\frac{1}{r\sin\theta}\frac{\partial\Psi}{\partial\phi} \\ &= \frac{1}{\sin\theta}\sum_{n=1}^{\infty}\sum_{m=0}^{n} m\left(\frac{R}{r}\right)^{n+2}\big(g_n^m \sin m\phi - h_n^m \cos m\phi\big)P_n^m(\mu). \end{aligned} \tag{20}$$

Following Rudenko (2001), we define the coordinate system such that the line-of-sight direction corresponds to the polar axis of the expansion. With this choice, the line-of-sight component of the field is given by

$$\begin{aligned} B_l &= B_r\cos\theta - B_\theta\sin\theta \\ &= \sum_{n=1}^{\infty}\sum_{m=0}^{n}(n-m+1)\left(\frac{R}{r}\right)^{n+2}P_{n+1}^m(\mu)\big[g_n^m \cos m\phi + h_n^m \sin m\phi\big]. \end{aligned} \tag{21}$$

To determine the coefficients in the expansion, we first multiply both sides of Equation (21) by $\cos m\theta$, and integrate over the surface of the sphere of radius R:

$$\begin{aligned} &\int_0^\pi \sin\theta d\theta \int_0^{2\pi} d\phi\, \cos m\phi P_{n+1}^m(\mu) B_l(R,\theta,\phi) \\ &= \sum_{n'=1}^{\infty}\sum_{m'=0}^{n'}\int_0^\pi \sin\theta d\theta \int_0^{2\pi} d\phi\, \cos m\phi\big(n'-m'+1\big)P_{n+1}^m(\mu)P_{n'+1}^{m'}(\mu) \\ &\quad \times \big[g_{n'}^{m'}\cos m'\phi + h_{n'}^{m'}\sin m'\phi\big] \\ &= \frac{4\pi g_n^m}{2n+3}\frac{(n+m+1)!}{(n-m)!}, \end{aligned} \tag{22}$$

which determines g_n^m. Next, we multiply both sides of Equation (21) by $\sin m\theta$, and again integrate over the surface of the sphere of radius R:

$$\begin{aligned} &\int_0^\pi \sin\theta d\theta \int_0^{2\pi} d\phi\, \sin m\phi P_{n+1}^m(\mu) B_l(R,\theta,\phi) \\ &= \sum_{n'=1}^{\infty}\sum_{m'=0}^{n'}\int_0^\pi \sin\theta d\theta \int_0^{2\pi} d\phi\, \sin m\phi\big(n'-m'+1\big)P_{n+1}^m(\mu)P_{n'+1}^{m'}(\mu) \end{aligned}$$

$$\times\left[g_{n'}^{m'}\cos m'\phi+h_{n'}^{m'}\sin m'\phi\right]$$

$$=\frac{4\pi h_n^m}{2n+3}\frac{(n+m+1)!}{(n-m)!} \tag{23}$$

to determine h_n^m.

Because observations are only available for the near side of the Sun, to implement this, it is necessary to make an assumption about the far side of the Sun. In order to ensure a zero monopole moment, it is convenient to make the field antisymmetric in some form. One convenient way to do this is to let $B_l(R,\pi-\theta,\phi)=B_l(R,\theta,\phi)$, where the front side of the Sun is assumed to lie in the range $0<\theta<\pi/2$. The associated Legendre functions have the property

$$P_n^m(-x)=(-1)^{(n+m)}P_n^m(x), \tag{24}$$

from which the expressions for the coefficients become

$$\begin{aligned}g_n^m&=\frac{(2n+3)(n-m)!}{4\pi(n+m+1)!}\int_0^{2\pi}d\phi\,\cos m\phi\\&\quad\times\left\{\int_{-1}^{0}d\mu\,P_{n+1}^m(\mu)+\int_0^1 d\mu\,P_{n+1}^m(\mu)\right\}B_l(R,\mu,\phi)\\&=\frac{(2n+3)(n-m)![1+(-1)^{n+m+1}]}{4\pi(n+m+1)!}\\&\quad\times\int_0^{2\pi}d\phi\,\cos m\phi\int_0^1 d\mu\,P_{n+1}^m(\mu)B_l(R,\mu,\phi),\end{aligned} \tag{25}$$

and similarly,

$$\begin{aligned}h_n^m&=\frac{(2n+3)(n-m)![1+(-1)^{n+m+1}]}{4\pi(n+m+1)!}\\&\quad\times\int_0^{2\pi}d\phi\,\sin m\phi\int_0^1 d\mu\,P_{n+1}^m(\mu)B_l(R,\mu,\phi).\end{aligned} \tag{26}$$

Note that the terms with $n+m$ even have $g_n^m=h_n^m=0$. This is a consequence of the boundary condition imposed for the far side of the Sun, which effectively reduces the number of independent terms by a factor of two.

References

Alissandrakis, C.E.: 1981, *Astron. Astrophys.* **100**, 197.

Altschuler, M.D., Newkirk, G.: 1969, *Solar Phys.* **9**, 131. DOI.

Bobra, M.G., Sun, X., Hoeksema, J.T., Turmon, M., Liu, Y., Hayashi, K., Barnes, G., Leka, K.D.: 2014, *Solar Phys.* **289**, 3549. DOI.

Bogdan, T.J.: 1986, *Solar Phys.* **103**, 311. DOI.

Centeno, R., Schou, J., Hayashi, K., Norton, A., Hoeksema, J.T., Liu, Y., Leka, K.D., Barnes, G.: 2014, *Solar Phys.* **289**, 3531. DOI.

Chapman, G.A., Sheeley, N.R. Jr.: 1968, In: Kiepenheuer, K.O. (ed.) *Structure and Development of Solar Active Regions*, *IAU Symposium* **35**, 161.

Gary, G.A., Hagyard, M.J.: 1990, *Solar Phys.* **126**, 21.

Giovanelli, R.G.: 1980, *Solar Phys.* **68**, 49. DOI.

Hoeksema, J.T., Liu, Y., Hayashi, K., Sun, X., Schou, J., Couvidat, S., Norton, A., Bobra, M., Centeno, R., Leka, K.D., Barnes, G., Turmon, M.: 2014, *Solar Phys.* **289**, 3483. DOI.

Ito, H., Tsuneta, S., Shiota, D., Tokumaru, M., Fujiki, K.: 2010, *Astrophys. J.* **719**, 131. DOI.
Jones, H.P.: 1985, *Aust. J. Phys.* **38**, 919.
Keller, C.U., The Solis Team: 2001, In: Sigwarth, M. (ed.) *Advanced Solar Polarimetry – Theory, Observation, and Instrumentation*, *Astron. Soc. Pac. Conf. Ser.* **236**, 16.
Leka, K.D., Barnes, G., Crouch, A.D., Metcalf, T.R., Gary, G.A., Jing, J., Liu, Y.: 2009, *Solar Phys.* **260**, 83. DOI.
Livshits, M.A., Rudenko, G.V., Katsova, M.M., Myshyakov, I.I.: 2015, *Adv. Space Res.* **55**, 920. DOI.
Pesnell, W.: 2008, In: *37th COSPAR Scientific Assembly*, *COSPAR, Plenary Meeting* **37**, 2412.
Petrie, G.J.D.: 2015, *Living Rev. Solar Phys.* **12**, 5. DOI.
Pope, T., Mosher, J.: 1975, *Solar Phys.* **44**, 3. DOI.
Riley, P., Linker, J.A., Mikić, Z., Lionello, R., Ledvina, S.A., Luhmann, J.G.: 2006, *Astrophys. J.* **653**, 1510. DOI.
Riley, P., Ben-Nun, M., Linker, J.A., Mikic, Z., Svalgaard, L., Harvey, J., Bertello, L., Hoeksema, T., Liu, Y., Ulrich, R.: 2014, *Solar Phys.* **289**, 769. DOI.
Rudenko, G.V.: 2001, *Solar Phys.* **198**, 5. DOI.
Sainz Dalda, A., Martínez Pillet, V.: 2005, *Astrophys. J.* **632**, 1176. DOI.
Sakurai, T.: 1982, *Solar Phys.* **76**, 301. DOI.
Scherrer, P.H., Schou, J., Bush, R.I., Kosovichev, A.G., Bogart, R.S., Hoeksema, J.T., Liu, Y., Duvall, T.L., Zhao, J., Title, A.M., Schrijver, C.J., Tarbell, T.D., Tomczyk, S.: 2012, *Solar Phys.* **275**, 207. DOI.
Schrijver, C.J.: 2007, *Astrophys. J. Lett.* **655**, 117. DOI.
Svalgaard, L., Duvall, T.L. Jr., Scherrer, P.H.: 1978, *Solar Phys.* **58**, 225. DOI.
Tsuneta, S., Ichimoto, K., Katsukawa, Y., Lites, B.W., Matsuzaki, K., Nagata, S., Orozco Suárez, D., Shimizu, T., Shimojo, M., Shine, R.A., Suematsu, Y., Suzuki, T.K., Tarbell, T.D., Title, A.M.: 2008, *Astrophys. J.* **688**, 1374. DOI.
Wang, Y., Sheeley, J.N.R.: 1992, *Astrophys. J.* **392**, 310. DOI.
Wieczorek, M.A., Meschede, M., Oshchepkov, I., Sales de Andrade, E.: 2016, *Zenodo*. DOI.